Int J Adv Manuf Technol (2013) 69:2569–2581
DOI 10.1007/s00170-013-5171-y

ORIGINAL ARTICLE

Microstructure and hardness of fiber laser deposited Inconel 718 using filler wire

Y. N. Zhang · X. Cao · P. Wanjara

Received: 28 February 2013 / Accepted: 10 June 2013 / Published online: 13 August 2013

Abstract A continuous wave 5 kW fiber laser welding system was used to deposit INCONEL® alloy 718 (IN718) layers in conduction mode by applying filler wire with a composition similar to the parent metal, which was extracted directly from a scrapped, service-exposed IN718 aerospace component. The quality of the deposits was characterized in both the as-deposited and fully heat-treated conditions in terms of the macrostructure, defects, microstructure, and hardness. Integral deposits with no visible porosity were obtained using the fiber laser deposition technique. In the as-deposited clad zone, weld metal liquation cracking led to the presence of minor microcracks in the lower layer beads near the layer interface. The crack healing behavior observed after post-clad heat treatment of the IN718 deposits supports the marked potential of using the laser deposition technique by filler wire addition to manufacture and repair/remanufacture superalloy components for aerospace applications.

Keywords Direct laser deposition · Fiber laser · Superalloy · IN718 · Filler wire

Abbreviations

ADed	As deposited
ASed	As-serviced
CZ	Cladding zone
HAZ	Heat-affected zone
PCHT	Post-clad heat treatment
PM	Parent metal
PMZ	Partially melted zone
STA	Solution treatment and aging

Y. N. Zhang · X. Cao (✉) · P. Wanjara
Structures, Materials and Manufacturing Laboratory, National Research Council Canada—Aerospace, 5145 Decelles Ave, Montreal, Quebec H3T 2B2, Canada
e-mail: Xinjin.cao@cnrc-nrc.gc.ca

1 Introduction

Additive manufacturing has become an emerging manufacturing and remanufacturing (repair) technique for aerospace materials such as INCONEL® alloy 718 (IN718) [1–3], particularly using a laser beam as the heating source. High-energy density laser welding is characterized by high processing speed and low overall heat input that minimizes the fusion zone and heat-affected zone (HAZ), and renders low distortion [4–7]. In the case of IN718, it was also reported that the HAZ microfissures, widely encountered during welding, can be avoided by using a low-power pulsing wave Nd:YAG laser [4, 8, 9] and a high-power CO_2 laser [4, 10]. In recent years, the innovative progress of disk and fiber lasers has enhanced the process capabilities over conventional CO_2 and Nd:YAG lasers due to their marked advantages including high energy efficiency, good beam quality, power scalability, flexible fiber beam delivery, small footprint, good process versatility, automation capacity, and low overall costs [11–14]. However, research and industrial experience with these relatively new laser systems are presently limited and of avid interest for technological evaluation and development.

During direct laser deposition, the filler material used is mainly fed in the form of powder or wire. Compared to powder feeding, the use of filler wire has several advantages including lower cost, higher material efficiency (less waste), lower contaminant pick-up (higher quality), lower oxidation (fewer defects), and higher deposition rate (productivity) [15, 16]. Also in deliberation of the availability of a wide range of filler wire materials and continuous precision wire feeding systems that have been developed/integrated for welding, the adaptation of filler wire for deposition is inherently less complex [17, 18]. To this end, satisfactory metal transfer can well be achieved when the filler wire is fed at an impingement angle of 30° and positioned to the exact edge of the molten pool [17].

As deposition of IN718 using a high-power fiber laser and filler wire feeding is an emerging technology, reported data

on the metallurgical and mechanical properties of the resultant IN718 deposits is limited and thus it is necessary to substantiate the suitability of this technology for aerospace component manufacturing and repair. Hence, this research work, which forms part of a larger collaboration on manufacturing technology development of Ni-based superalloys, was undertaken to investigate the viability of additive manufacturing and repairing IN718 using a continuous wave fiber laser with filler wire addition. To simulate industrial conditions, the deposits were built on parent metal (PM) substrates extracted from serviced IN718 aerospace components. The deposits were then evaluated in terms of macrostructure, microstructure, defects, and hardness (Vickers, Brinell, and Rockwell) in the as-deposited (ADed, i.e., non heat treated) and the post-clad heat-treated (PCHTed, i.e., solution heat treated and aged) conditions.

2 Experimental

The laser equipment used consisted of an IPG Photonics 5 kW continuous wave solid-state Yb-fiber laser system (YLR-5000) equipped with an ABB robot. A collimation lens of 150 mm, a focal lens of 250 mm, and a fiber diameter of 600 μm were employed to produce a nominal focusing spot diameter of approximately 1.0 mm. In this study, a positive defocusing distance of +12 mm was used to obtain a laser power density of 2×10^4 W/cm^2. The fiber laser beam with a wavelength of about 1.07 μm was positioned on the top surface of the deposits. The laser head was inclined 2–3° both along the lateral side and from the vertical position towards the cladding direction to avoid any damage to the equipment from the laser beam reflection. To protect the molten metal during deposition, the clad zone (CZ) was shielded using two streams of Ar gas flow. One stream of Ar flow at a rate of 30 cfh was directed towards the cladding direction at an angle of 18–20° to the deposition surface while the other was directed opposite to the cladding direction at a rate of 20 cfh. The IN718 filler wire, approximately 0.89 mm in diameter, was axially fed from the cladding direction and intercepted the laser beam on the deposit surface. Each layer was deposited along a single cladding direction.

In this work, coupons of the PM substrates were extracted from a scrapped, service-exposed IN718 aerospace component that were solution heat treated and aged (STAed) and hereafter referred to the as-serviced (ASed) condition. These ASed PM substrates were employed for process development and optimization, as well as direct laser deposition of multi-bead and multi-layer coupons. After laser deposition, selected coupons were STAed. The solution heat treatment was carried out in vacuum at a temperature of 1,750±25 °F (954 °C) for 1 h in the presence of inert Ar gas and then cooled down (with Ar) at a minimum rate of 30 °F·min^{-1} to a temperature of 1,000 °F (538 °C) followed by rapid cooling in Ar. The aging consisted of the following steps: heating up to 1,350±25 °F (732 °C), soaking for 8 h, furnace cooling under Ar to 1,110±25 °F (599 °C) and holding for 8 h, and finally Ar quenching.

The metallographic samples were characterized in both the ADed and PCHTed conditions. Each direct laser deposited coupon was sectioned using a precision cut-off saw to extract specimens for metallographic examination and hardness evaluation. After sectioning, the specimens were mounted, ground, and polished to a surface finish of 0.04 μm, followed by etching in a solution of 0.5 % nital (0.5 ml nitric acid in 100 ml ethanol). Electrolytic etching was usually used to reveal the microstructural constituents. Specimens were immersed in a saturated solution of 10 g oxalic acid in 100 ml distilled water. A voltage of 6 V was applied for 8–20 s, depending on the specimen conditions (i.e., ADed or PCHTed). Optical microscopy (Olympus GX-71) coupled with image analysis software (AnalySIS) was used to examine the weld bead geometry and characterize the macro- and microstructural features (including defects such as pores and cracks).

The microhardness was measured using a Struers Duramin A300 machine with a fully automated testing cycle (stage, load, focus, and measure). A load of 300 g was applied using a load cell with closed-loop circuit control and the hardness profiles were determined across the deposits using an indent interval of 0.2 mm and a dwell period of 15 s. It is noteworthy that according to ASTM E384, the spacing between two adjacent indentations must be at least three times the diagonal length of the indentation. Hence, the spacing between two adjacent indentations during microhardness testing was suitably selected to avoid any potential effect of the strain fields caused by adjacent indentations. Also, bulk hardness measurements were conducted using a Zwick ZHU250 universal tester and a Wilson Rockwell tester to respectively evaluate the Brinell and Rockwell hardness of the deposits.

3 Results and discussion

3.1 Macrostructure

Figure 1 shows the transverse sections of some single and multi-bead welds. As revealed in Fig. 1a, a wide (top bead width of 3.9 mm) and shallow (penetration depth of 0.6 mm) single bead is obtained. During laser welding, a weld bead with an aspect ratio of 1.2 or less is usually thought to form in conduction mode, i.e., in a similar manner to conventional fusion welding processes [19]. In conduction-mode welding, the surface of the material is heated above its melting point but below its vaporization temperature. Fusion occurs only by heat conduction through the molten weld pool. In contrast, another welding mode (i.e., keyhole) has been widely used for

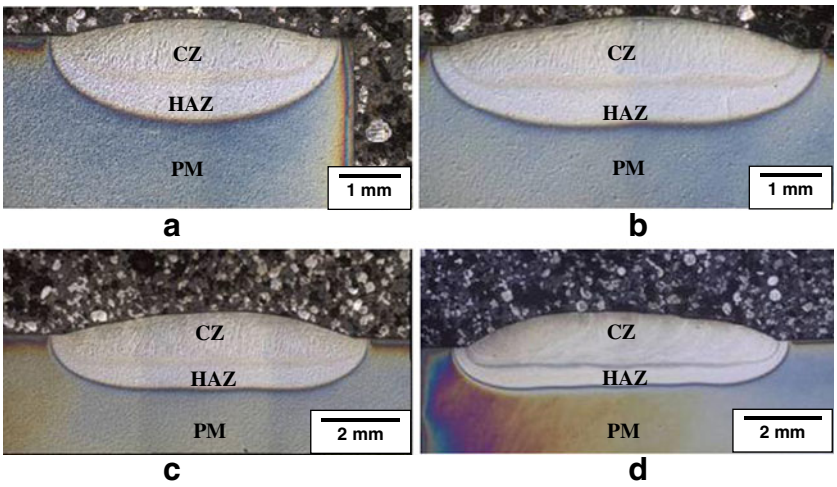

Fig. 1 Single-layer laser deposits in ADed condition: **a** 1, **b** 2, **c** 3, and **d** 5 beads

laser beam welding. In keyhole mode, a higher power density is used to cause local vaporization. Thus a narrow and deeply penetrated vapor cavity, with an aspect ratio higher than 1.2, is usually formed by multiple internal reflections of the laser beam. Keyhole-mode welding usually results in better energy coupling, higher penetration, and higher welding speed that are necessary for economic justification. Therefore, most applications of laser welding are focused on the deep penetration keyhole-mode process. The basic difference between the two modes is that the surface of the weld pool opens up to allow the laser beam to enter the molten weld pool in keyhole welding but remains unbroken in conduction mode [20]. As a consequence, the conduction mode offers lower penetration depth, less perturbation to the weld pool, and a much lower tendency to entrap solid surface oxides and gases. These advantages are all beneficial for direct laser deposition for component manufacture and/or repair.

The single-bead weld obtained in conduction mode, as shown in Fig. 1a, had a crown height of 0.29 mm and a dilution ratio (percentage of melted area in the parent metal over the total melted area) of 72.2 %. Under similar conditions, multi-bead welds were deposited in a single layer, as illustrated in Fig. 1b–d. For both the single- and multi-bead welds, the CZ and the HAZ can be clearly differentiated, as demarcated in Fig. 1. Examination of the single-bead deposit indicated that a HAZ width of 0.33 mm was present on both sides of the top surface. In contrast, the maximum HAZ width (0.82 mm in Fig. 1a) appeared at the bead root. The narrow HAZ is due to the low heat input and localized rapid heating and cooling during laser deposition. No porosity was observed in the CZ. Also no evidence of macrocracks was found in the CZ or the HAZ.

On the basis of these integral multi-bead single-layer welds, a multi-bead and multi-layer deposit (roughly 30×35×200 mm in size) was manufactured, as shown in Fig. 2. Macroscopic examination of the deposit revealed three distinct regions, i.e., PM, HAZ (including partially melted zone, PMZ), and CZ, which will be discussed in detail below. As indicated in Fig. 2, the size of the HAZ between the PM and the multi-bead, multi-layer deposit remains very narrow (<1 mm) in spite of the heat accumulation during laser deposition. Similar to the multi-bead single-layer welds, no evidence of porosity or macrocracks was observed in the CZ and the HAZ of the multi-bead, multi-layer deposit.

3.2 Microstructure

3.2.1 Parent metal

Figure 3 shows the microstructure of the IN718 PM in the ASed and PCHTed conditions. The PM in both conditions mainly consisted of equiaxed austenitic γ grains, globular Ni_3Nb-δ precipitates, Nb-rich MC particles and, as well known, the age-hardening/strengthening phases γ' and γ'' in the grains. The γ grains are a face-centered-cubic (fcc) Ni-based continuous matrix phase with solid solution elements such as Co, Cr, Mo, and W. Randomly distributed Nb-rich MC type primary carbides and carbonitrides with sizes up to 10 μm were also observed at the γ matrix grain boundaries. Globular Ni_3Nb-δ precipitates, approximately 2–5 μm were distributed within the grains and at the γ grain boundaries and their presence is attributed to the multiple thermal cycles during service of the IN718 aerospace component (from which the PM substrates were extracted) [1, 21]. An average γ grain size of 14 μm (ASTM 9.0–9.5) was determined for the ASed condition (Fig. 3a). After PCHTed, slight coarsening of the γ grains (approximately 17 μm or ASTM 8.0–8.5) was observed, as shown in Fig. 3b. It is noteworthy that the re-aging heat treatment may also cause coarsening or re-precipitation of the strengthening phases, such as γ' and γ'' in the grain interior of the γ matrix. Due to the formation of γ/γ' eutectic, γ' can also form in the interdendritic or intergranular regions [1].

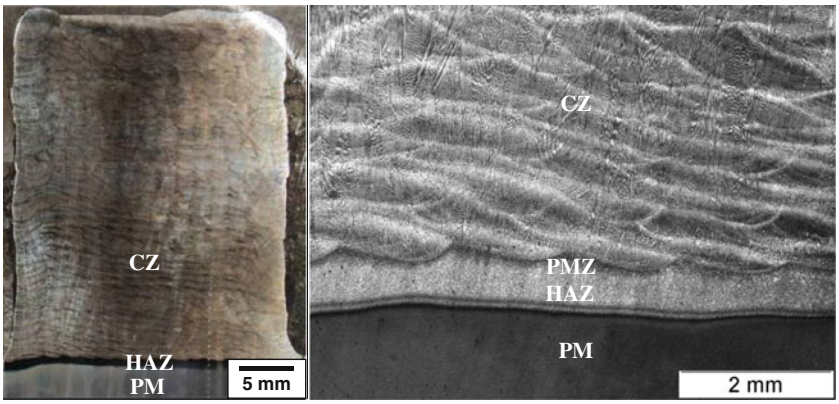

Fig. 2 A multi-layer coupon with 15 beads/layer by 45 layers in ADed condition

3.2.2 HAZ between PM and CZ

Compared to the PM, more complex microstructures were observed in the HAZ between the PM and the CZ. The typical microstructure in the HAZ of a single-bead weld and a multi-bead, multi-layer deposit is shown in Figs. 4 and 5, respectively. Specifically, as illustrated in Figs. 1a and 4a, the HAZ (including the PMZ) between the PM and the CZ of a single-bead weld was observed to be narrow (<0.8 mm) and without significant grain growth relative to the PM. The size of the HAZ was noted to increase slightly (~1.0 mm) for the multi-bead, multi-layer deposit. In the ADed condition, the HAZ between the PM and the CZ of the multi-bead multi-layer deposit (Fig. 5) had a similar microstructure to that of the single-bead weld (Fig. 4) and mainly consisted of a γ matrix, globular Ni_3Nb-δ precipitates, Nb-rich MC type primary carbides and carbonitrides, as well as the well-known strengthening phases, γ' and γ'' in the γ grains (Figs. 4e and 5e). In addition, needle-like Ni_3Nb-δ precipitates were also apparent [1, 21], at the grain boundaries in the HAZ. With increasing temperature towards the CZ, however, some variations in the microstructure are noted in the HAZ. As shown in Figs. 4b–d and 5a and c, some large "particles" were only observed in the PMZ of the HAZ very close to the CZ. These are thought to be a Nb-rich phase (similar to the composition of the Ni_3Nb-δ), formed as a Nb-rich liquid "particle" structure due to the phase transformation of γ'' to Ni_3Nb-δ and the dissolution of the Ni_3Nb-δ precipitates at the heating stage during laser deposition [1, 21]. The dissolution of the Ni_3Nb-δ particles is due to the high temperature experienced in the PMZ that can be beyond the solidus of the Ni_3Nb-δ phase (995 °C as shown in Fig. 6a). With increasing proximity to the CZ, the increasingly higher temperatures led to the formation of larger Nb-rich liquid "particle" structure, as shown in Figs. 4d and 5c. In contrast, the HAZ close to the PM was similar in microstructure to that of the PM due to the lower local temperatures experienced, which in turn may not have generated sufficient heat to dissolve the Ni_3Nb-δ phase.

In the PCHTed condition, a large amount of the needle-like Ni_3Nb-δ precipitates was observed in the PMZ close to the CZ, as shown in Fig. 5d. These needle-like Ni_3Nb-δ precipitates in the PCHTed condition most likely precipitated from the liquid "particle" (present in the ADed condition) during the solution heat treatment [21], as shown in Figs. 5d and 6b and c. In this work, the solution heat treatment was carried out at 954 °C, which is lower than the solidus temperature of the Ni_3Nb-δ precipitates (995 °C as shown in Fig. 6a), indicating that the heat input conditions were insufficient to dissolve all globular Ni_3Nb-δ precipitates in the HAZ and PM. Hence, after the PCHT, the HAZ near the PM (Fig. 5f) has a similar microstructure to the PM, consisting of the γ matrix, globular Ni_3Nb-δ, Nb-rich MC type primary

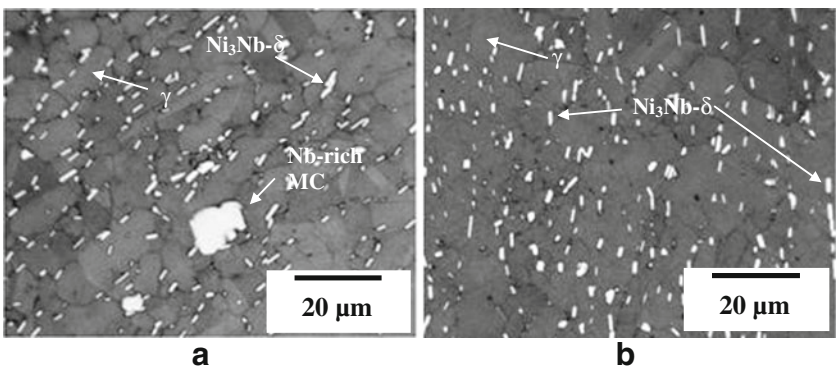

Fig. 3 Microstructures of the PM IN718 in **a** ASed and **b** PCHTed conditions

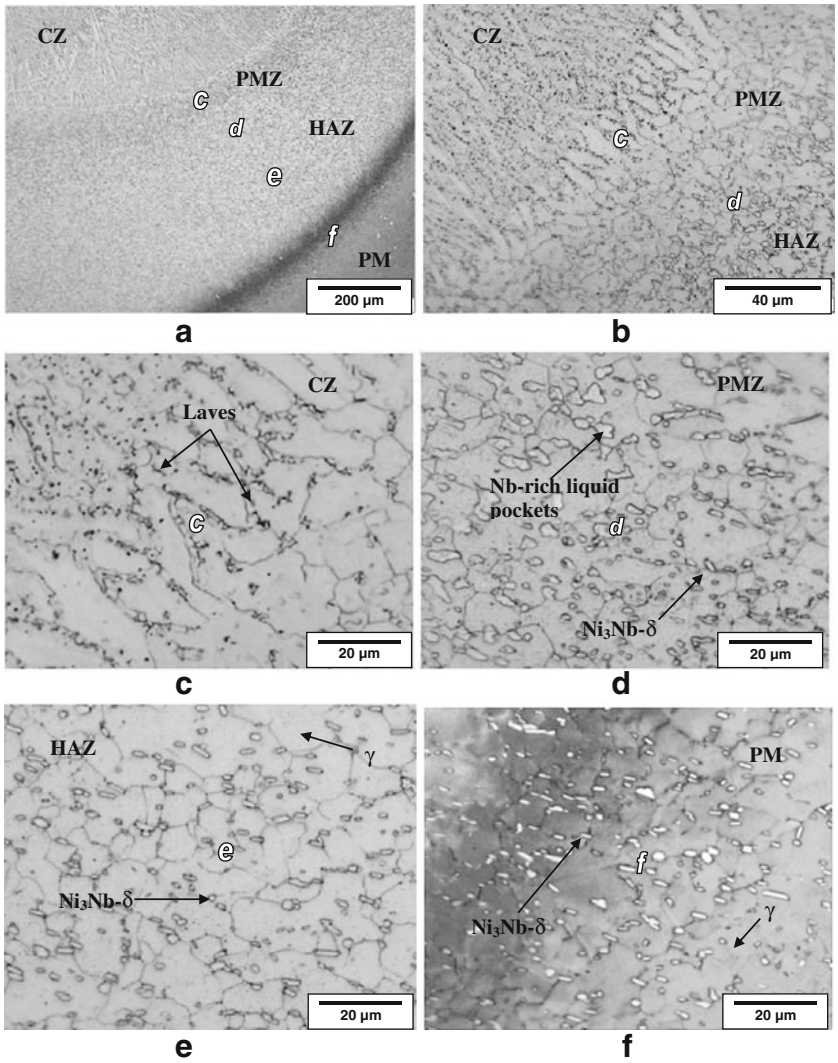

Fig. 4 HAZ (including PMZ) between the PM and the single bead weld shown in Fig. 1a in the ADed condition

carbides and carbonitrides, as well as, undoubtedly, the γ' and γ''.

3.2.3 Clad zone

In the CZ, typical elongated dendritic structures were observed as shown in Fig. 7. IN718, being a heavily alloyed material, solidifies in a dendritic mode after laser deposition. The dendrites extend from the layer boundary to the bead center. In laser deposition, the relatively rapid cooling rate leads to fine dendritic structures in the CZ. As shown in Fig. 7, Laves and other hard phases in interdendritic regions are selectively etched (darkened) compared with the dendritic cores. The dendrites were observed to be finer and more equiaxed in each bead center (Fig. 7a and c) but became slightly coarser and columnar near the bead interface (Fig. 7b and d). Fine equiaxed dendritic growth in the weld interior gave rise to more, but smaller and well-separated, interdendritic regions, leading to the formation of relatively fine and discrete Laves particles. In contrast, columnar dendritic growth adjacent to the bead interface resulted in fewer, but larger and more continuous, interdendritic regions, and thereby coarser and more interconnected Laves particles [4, 5].

As is well known, the cooling rate over the solidification temperature range can be estimated using the following equation [23, 24]:

$$\lambda s = k_s \Theta^n \tag{1}$$

where Θ is the cooling rate over the solidification temperature range, and k_s and n are constants. The CZ in Fig. 7 consists of a cellular-dendritic microstructure with an average secondary dendrite arm spacing, λs, of about ~3.3±0.5 μm, as measured near the bead interfaces. Using the values of $k_s = 4.7 \times 10^{-2}$ $mmK^{1/3}\ s^{-1/3}$ and $n = -0.4$, as experimentally determined for a nickel-based superalloy (IN738) [23], the cooling rate near the bead interface is estimated to be ~971 K/s. This cooling rate is quite similar to that obtained for CO_2 laser welded Haynes 282 alloy where the secondary dendrite arm spacing and the cooling rate within the fusion zone are 3.1±0.6 μm and

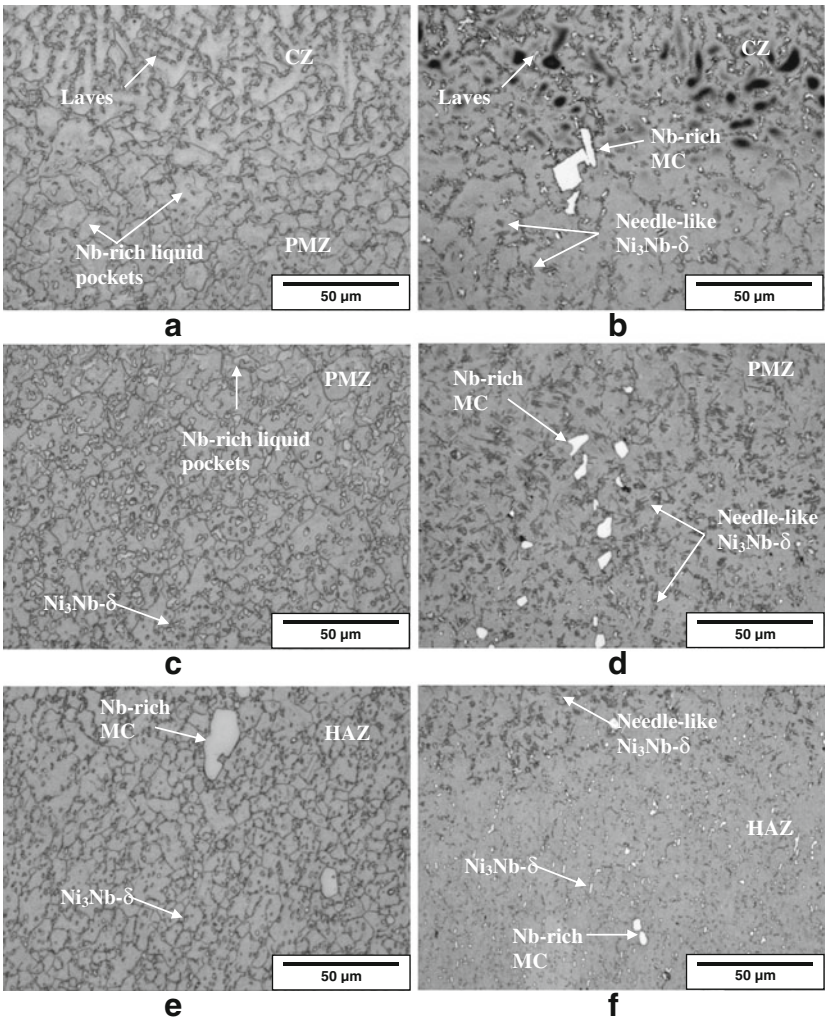

Fig. 5 HAZ between the PM and the multi-bead, multi-layer deposit shown in Fig. 2 in the ADed (**a**, **c**, **e**) and PCHTed (**b**, **d**, **f**) conditions

1168 K/s, respectively [24]. The slightly lower cooling rate obtained in this work is partly due to the heat accumulation during laser deposition. It is noteworthy that the cooling rate is obtained over the solidification temperature range near the bead interface in this study. In contrast, the bead center has a higher cooling rate as compared with the bead interface [25]. However, the cooling rate obtained in laser deposition (971 K/s) is much higher than that in gas tungsten arc welding (500 K/s) [26].

Solidification in IN718 starts with the primary liquid → γ reaction, causing the enrichment of Nb, Mo, Ti, and C in interdendritic liquid. The subsequent liquid → (γ+NbC) eutectic reaction consumes most of carbon available in the material until another eutectic type reaction liquid → (γ+Laves) occurs, terminating the solidification process [4, 6]. The detrimental Laves phase (hexagonal $MgZn_2$ type) is an unavoidable terminal solidification phase in IN718. However, solidification conditions can strongly influence the extent of Nb segregation and hence the amount of Laves phase. The Laves particles are usually rich in Nb, Ti, Mo, Si, and lean in Fe, Cr, and Ni as compared to the PM [4]. Both the amount of the Laves phase and the Nb segregation are a function of solidification conditions. Compared with conventional arc welding processes, the higher cooling rate experienced in laser cladding may result in a lesser extent of Nb segregation because of the insufficient time for solute redistribution [25, 26]. Hence, fewer Laves particles and a lower Nb concentration in these Laves particles are typically obtained [5].

In laser deposition, the relatively rapid cooling rate can also extend solute solubility, which reduces the extent of segregation and forms less eutectic constituents. During solidification, the elements Nb, Ti, and Mo accumulate at the front of the liquid/solid interface and segregate into interdendritic areas where carbide (NbC, fcc) and Laves particles may form [8]. The γ and NbC eutectic can be suppressed during rapid cooling [8]. The interdendritic Nb-rich Laves phase, that has morphologies related to the dendritic structure, may form an interconnected network [8], as shown in Fig. 7. As observed in Fig. 7b and d, the Laves particles in columnar dendritic regions were interconnected and became slightly coarser than those in the equiaxed dendritic regions. In addition, the amount of the Laves phase was slightly higher in the columnar

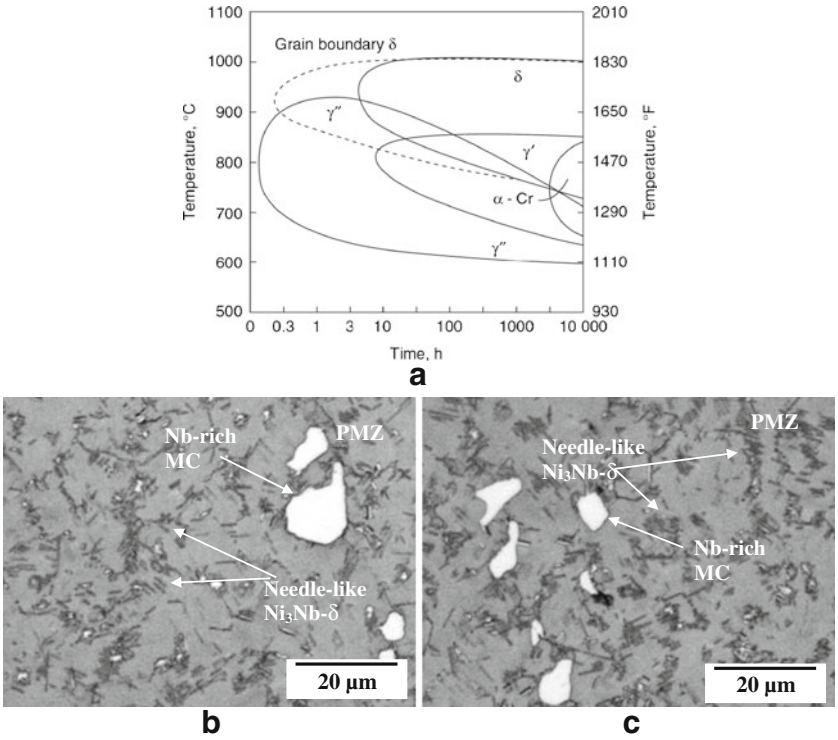

Fig. 6 **a** TTT diagram for IN718 [1, 22], and **b**–**c** needle-like δ precipitates in the PMZ of the HAZ between the PM and the multi-layer deposit in Fig. 5d in the PCHTed condition

dendritic regions near the bead interface (Fig. 7b) than that in the fine equiaxed dendritic portions (Fig. 7a). However, the average Nb concentration in the Laves particles in both columnar and equiaxed regions should be similar [4].

It is well known that the formation of the Laves phase can (1) deplete principal alloying elements required for hardening from the matrix, (2) represent a weaker CZ microstructure between the Laves phase and the matrix interface by segregation of useful strengthening alloying elements, and (3) act as preferential sites for easy crack initiation and propagation [1, 4, 6]. The inherent brittle nature of the Laves phase leads to poor tensile ductility, fracture toughness, and fatigue and creep rupture properties in

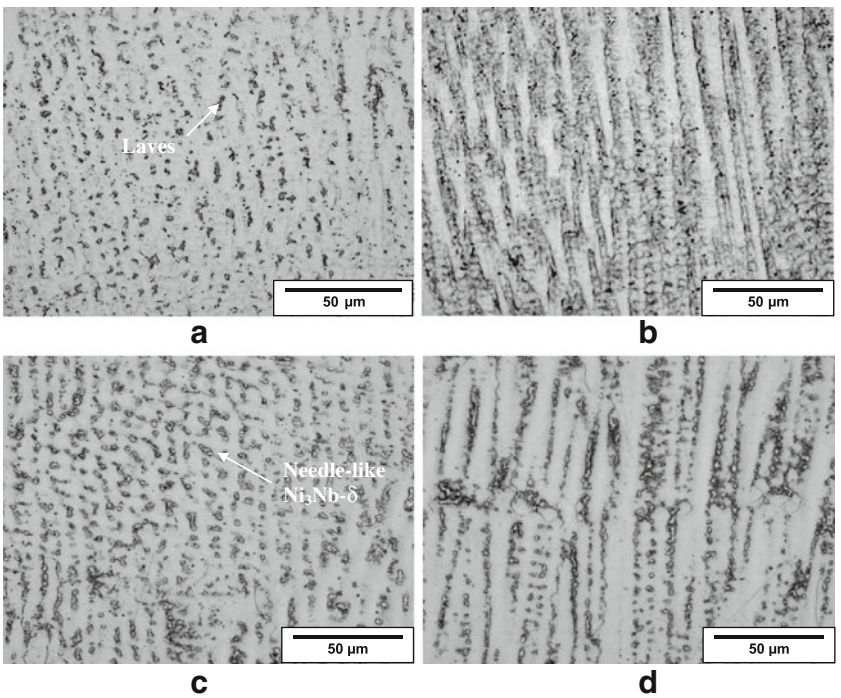

Fig. 7 Microstructures of the CZ **a** at a bead center and **b** near a bead interface in ADed condition, **c** at a bead center, and **d** near a bead interface in PCHTed condition

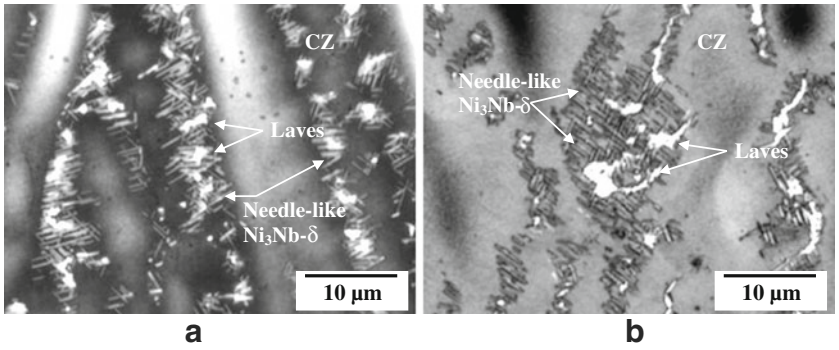

Fig. 8 Needle-like δ precipitates around Laves particles in the PCHTed condition

IN718 welds and castings [4–6, 27, 28]. Therefore, the Laves phase is detrimental and hence should be carefully controlled. Compared with the ADed condition (Fig. 7a and b), less Laves particles are observed in the interdendritic regions after the PCHT (Fig. 7c and d). Thus, the PCHT results in considerable dissolution of the Laves particles at a solution temperature of 954 °C. In this case, less interdendritic constituents were observed, as shown in Fig. 7c and d. Furthermore, the formation of the needle-like Ni_3Nb-δ precipitates around the Laves particles in the interdendritic regions is due to the partial dissolution of the Laves particles during the PCHT during the heating stage, as demonstrated in Fig. 8. However, the solution treatment conducted at 954 °C did not completely dissolve the Laves particles. The δ phase is an

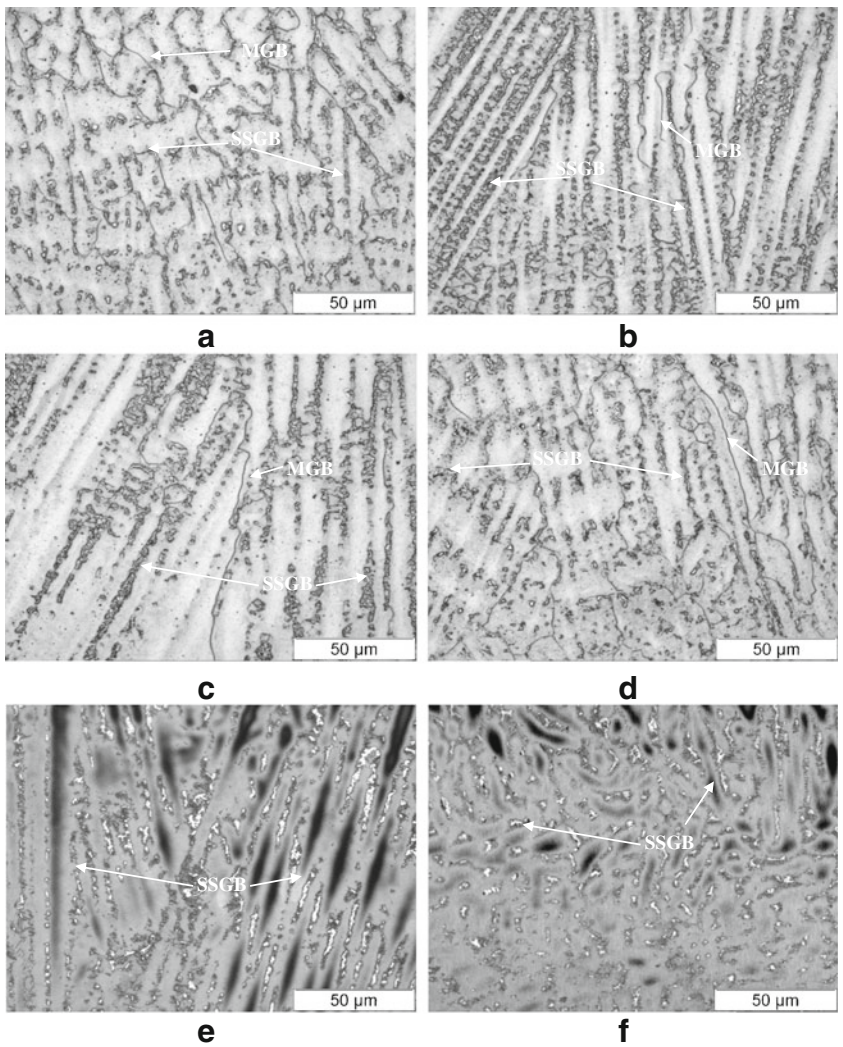

Fig. 9 Migrated grain boundaries (MGBs) in the CZ **a**–**d** obtained on the ADed and **e**, **f** without MGB in the PCHTed conditions

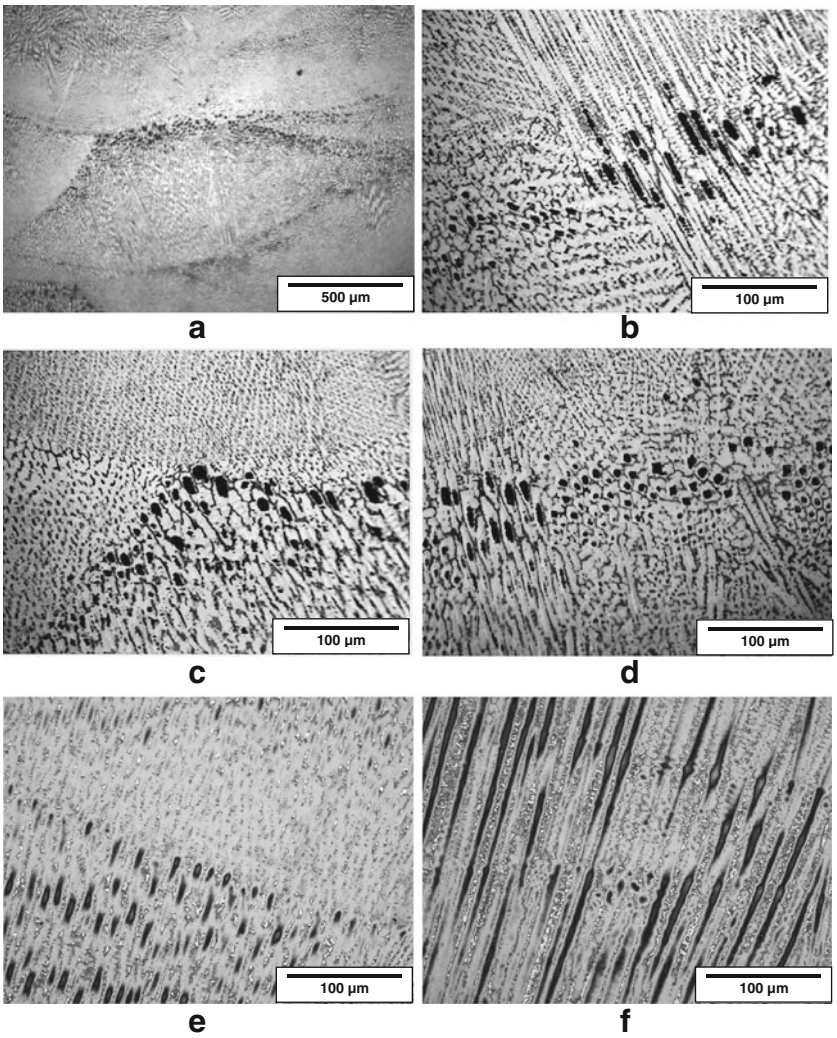

Fig. 10 Preferred corrosion in the dendritic cores near the bead/layer interfaces in the CZ **a**–**d** in the ADed and **e**, **f** in the PCHTed conditions

equilibrium Ni_3Nb precipitate with an orthorhombic crystal structure, which requires about 6–8 % Nb and precipitates in the range of 860–995 °C [4, 29], as shown in Fig. 6a.

Table 1 List of partition coefficients, maximum solid solubilities, and terminal eutectic temperatures [1]

System	K	Maximum solubility (wt.%)	Terminal eutectic temperature (°C)
Ni-P	0.02 (P in Ni)	0.32 P	870
Ni-S	0 (S in Ni)	0 S	637
Ni-B	0.04 (B in Ni)	0.7 B	1,093
Ni-Si	0.7 (Si in Ni)	8.2 Si	1,143
Mo	0.82 (Mo in IN718)	–	–
Al	1.0 (Al in IN718)	–	–
Ti	0.69 (Ti in IN718)	–	–
Si	0.67 (Si in IN718)	–	–
Lave+γ	0.48 (Nb in IN718)	9.3 Nb	1,200
NbC+γ		–	1,250

During solution heat treatment, the interdendritic regions become enriched in Nb due to the dissolution of Laves particles, which may cause an accumulation of 6–10 % Nb or more, and thus Ni_3Nb-δ particles may form in these regions where the Nb concentration is more than 10 % [4]. Therefore, during the solution heating treatment, locally some regions around the Laves particles in the weld metal will have a sufficient Nb concentration to incite the formation of the needle-like δ phase. The morphology of the needle-like Ni_3Nb-δ precipitates in the CZ is similar to that in the PMZ of the HAZ and they both were formed during solution heating treatment. However, the needle-like Ni_3Nb-δ particles were formed due to the partial dissolution of the Laves particles in the CZ, but precipitated from the liquid "pocket" structure in the PMZ of the HAZ.

As shown in Fig. 9, three distinct types of grain boundaries can be observed in the deposited layers under optical microscopy. They are the (1) solidification grain boundary (SGB), (2) solidification subgrain boundary (SSGB), and (3) migrated grain boundary (MGB) [1, 30]. The SSGB is the

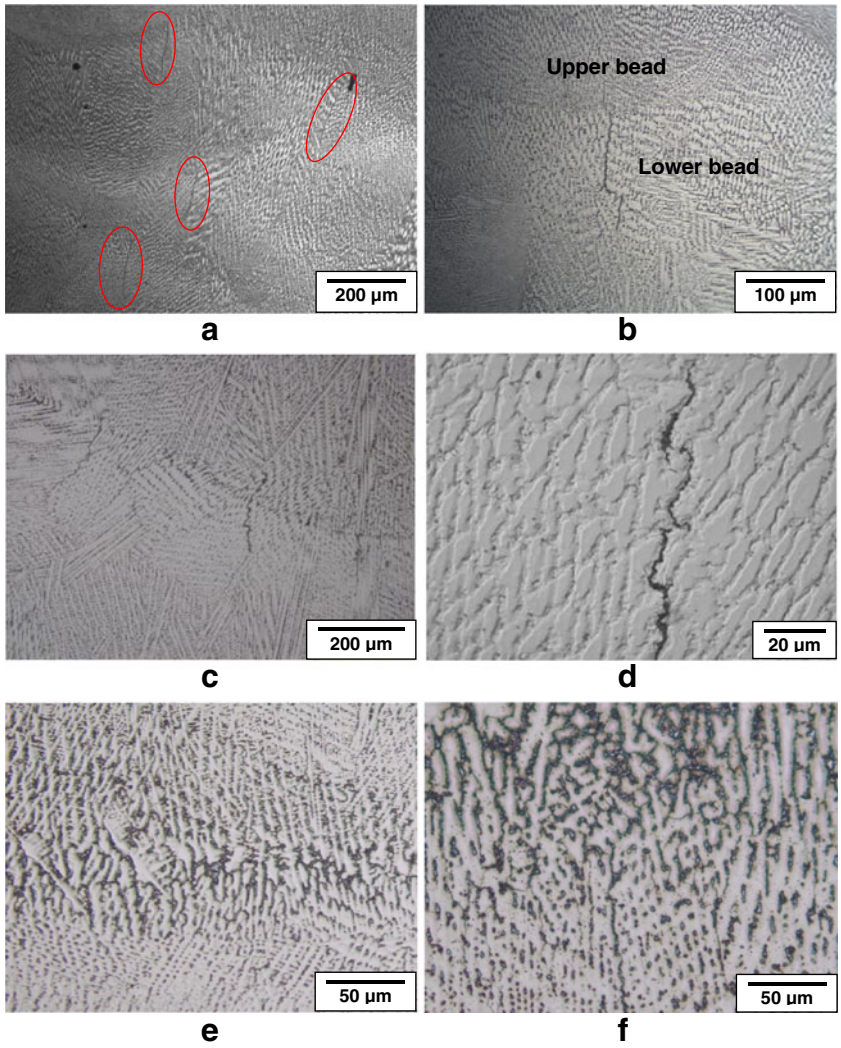

Fig. 11 Weld metal liquation cracks in **a**–**d** ADed and **e**–**f** PCHTed condition

finest structure resolvable using optical microscopy and represents the low angle boundaries separating the various morphological forms of solidification, such as cells, dendrites, and cellular dendrites. The SGBs are formed at the intersections of packets of SSGBs with different grain growth directions and therefore represent high-angle grain boundaries. In contrast, the MGBs were frequently observed in the CZ in the ADed condition (Fig. 9a–d) but invisible in the PCHTed condition (Fig. 9e and f). These result from the migration of the high angle component of the SGB in the solid-state, either immediately following solidification or during deposition. Since the SGB tends to be relatively tortuous due to the nature of its formation, there is a natural driving force for this boundary to move and straighten [30]. The boundary

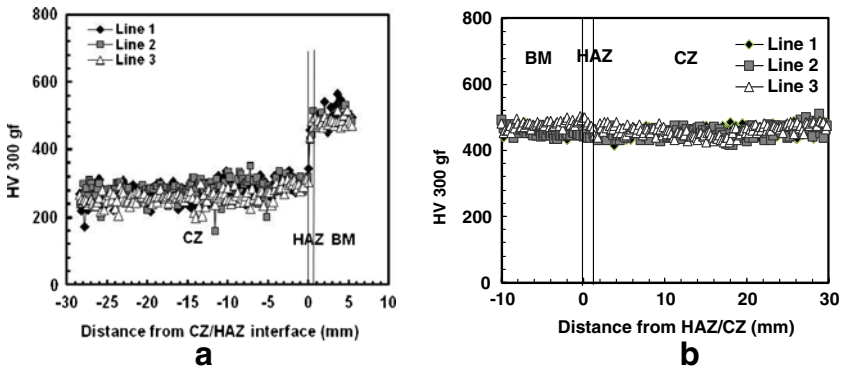

Fig. 12 Hardness distributions in **a** ADed and **b** PCHTed conditions

Table 2 Average microhardness values

Condition	Hardness (HV) at testing load of 300 g, and duration of 15 s		
	CZ	HAZ	PM
ADed with ASed IN718 PM	275±30	417±73	488±21
PCHTed with ASed IN718 PM	457±15	460±19	463±16

A standard deviation value indicated

may be pinned within the SGB by NbC or Laves particles that form along the SGB during the final stages of solidification or by NbC or Laves particles swept into the boundary from the molten pool.

As shown in Figs. 9 and 10, preferred corrosion often occurs at the dendrite cores near the bead interfaces in the CZ due to lower Mo content. Mo has a low value for the equilibrium distribution coefficient k (0.82 for IN718 as indicated in Table 1) and a negligible solid state diffusion coefficient ($D_o = 1 \times 10^{-4}$ m^2/s) [1], indicating that more Mo will segregate at the grain boundaries and, thus, resist the corrosion due to its high electrochemical potential. During chemical etching, therefore, dendrite cores are selectively corroded and lead to the formation of some small pits at the bead centers near the bead/layer interfaces. After PCHT, preferred corrosion still occurs in the dendrite cores, as shown in Fig. 10e and f, indicating that Mo has not been fully homogenized due to the extremely low diffusion coefficient in the solid state. The preferred corrosion occurring in the dendrite cores during electrolytic etching were also observed in laser welded IN718 [6].

3.3 Defects

Microfissures were not observed by optical microscopy in the HAZ between PM and CZ in both ADed and PCHTed conditions due to the fine matrix grains, the absence of the impurity elements (such as B, P, and S) and Laves phases in the ASed PM, and the low heat input used in the conduction-mode laser deposition process. In contrast, in the CZ, weld metal liquation cracking was frequently observed in the lower beads near the interfacial layer in ADed condition, as shown in Fig. 11a and b. This region of the lower beads acts as the HAZ of the adjacent upper layer beads that are deposited subsequently. Therefore, these microcracks are quite similar to the HAZ microfissures or liquation cracks, as widely encountered in IN718 welds. These microcracks are observed in the multi-pass depositions where the earlier deposited beads become the HAZ of the subsequent passes and thus are usually termed as weld metal liquation cracking [1]. As shown in Fig. 11a–d, weld metal liquation cracking occurs in the lower beads near the interfacial area but the cracks then propagate along the grain boundaries and even extend into the upper newly deposited layer'. After PCHTed, the absence of weld metal liquation cracking at the interfacial area, as observed in Fig. 11e and f, can be attributed to healing.

In general, grain boundary melting and liquation cracking can occur by two basic mechanisms: segregation and penetration [1, 31, 32]. In the segregation mechanism, solute and/or impurity elements segregate into the grain boundaries due to the low equilibrium distribution coefficients and, thus, suppress the local melting temperature of the grain boundary. Table 1 summarizes the partition coefficients, maximum solid solubilities, and terminal eutectic temperatures of some impurity elements and low melting point eutectics, including Laves or carbides phases. As shown in Table 1, the impurity elements such as B, S, and P have extremely low partition coefficients and, thus, easily segregate to the grain boundaries, promoting grain boundary cracking. In the penetration mechanism, constitutional liquation or local melting may occur in the microstructure at the elevated temperature [1]. Then the liquid penetrates and wets the grain boundaries, leading to the grain boundary being covered by a liquid film.

As discussed above, the CZ of the laser deposited precipitation-strengthened IN718 has a typical cast structure in the as-deposited condition, i.e., both Nb-rich carbides and Laves phase form during the final stages of solidification. For cast IN718, it is well known that liquation cracking is dominated by the melting of the Laves phase rather than constitutional liquation of the Nb-rich carbides since the former precipitates at a lower temperature [1] and the latter has a much lower amount, as indicated in Fig. 7. When the earlier deposited weld metal is reheated to a high temperature by subsequent laser deposition, the SGBs in the lower beads

Table 3 Hardness of IN718

Hardness	ASed PM	Clad zone	AMS 5596K sheets and plates (STAed)	AMS 5663M bars, forgings, flash welded rings, and stock for forgings or flash welded rings (STAed)
HBW 2.5/62.5	391 in the ASed condition	237 in the ASed condition		≥331 HB
HRC	45.7 in ASed condition; 42.5 in PCHTed condition	23.6 in the ASed condition; 41.6 in the PCHTed condition	≥36 (STAed)	

(Fig. 9a–d) adjacent to the layer interface may remelt, producing a liquated boundary similar to that present at the end of solidification. The reheating may also promote grain growth, resulting in the formation of MGBs along which liquation and even cracking can occur [1, 30].

After PCHTed, the weld metal liquation cracking was healed probably due to several reasons: (1) less Laves phase available due to its partial dissolution at the heating stage during the solution heat treatment, (2) improved strength due to the release of Nb into the matrix caused by the partial dissolution of the Laves phase at the heating stage and the precipitation of the γ'' strengthening phases at the cooling stage of the solution heat treatment, and (3) thermal strains and shrinkage stresses caused by rapid solidification that can be released during the PCHT [1].

Furthermore, lower heat inputs are also favorable for minimizing the weld metal liquation cracking due to the smaller widths of the PMZ. Cracking of any form cannot occur without some levels of tensile strain. The tensile strains in the CZ will develop due to residual stresses mainly from solidification shrinkage. Low heat input combined with low restraint during cladding helps to reduce the level of the tensile strain. In multi-pass welding/deposition, a process of using a greater number of smaller beads is beneficial because it can reduce the heat input, residual stress, and shrinkage strain [1].

3.4 Hardness

Typical Vickers microindentation hardness profiles across the deposits are shown in Fig. 12 and the average values are given in Table 2. The PM in the ASed condition has an average value of approximately 488 HV. The CZ hardness (275 HV) in the ADed condition is much lower than that in the ASed PM (488 HV), as shown in Fig. 12a and Table 2. The thermal cycle occurring during laser cladding may dissolve the principal strengthening phase γ'', which has a dissolution temperature of around 650 °C (in Fig. 6a). The hardness in the HAZ (417 HV) between the PM and CZ was found to drop from the ASed PM to the CZ in the ADed condition. This is due to the dissolution of the strengthening γ'' precipitates in the HAZ. It is noteworthy that the HAZ was relatively narrow in size and the hardness value is difficult to measure precisely, as indicated by the high standard deviation (73) in Table 2.

As shown in Fig. 12b, the CZ has a similar hardness to the fully heat-treated PM after PCHT. The increase in the CZ hardness is related to the re-precipitation of γ''. Laves phase and needle-like δ phase predominately consume the Nb originally present in the CZ, thereby reducing largely the Nb available for the precipitation of γ''. Therefore, the amount of Nb available for γ'' precipitation is considerably lower in the CZ, as compared to that in the PM [4]. The hardness of the CZ in PCHTed condition (457 HV) is much higher than that in the ADed condition (275 HV) due to the higher content of Nb available for γ'' precipitation (as a result of the considerable dissolution of the Laves phase). In contrast, the CZ hardness in the PCHTed condition is just slightly lower than that in the ASed PM (463 HV) due to the presence of Nb-rich Laves in the CZ that lowers the amount of Nb available for γ'' precipitation. The Vickers hardness results are consistent with the values of Brinell and Rockwell hardness measurements as obtained for the ASed PM and the clad IN718 in both the ADed and PCHTed conditions (Table 3).

4 Conclusions

Weld metal liquation cracking is frequently observed in the lower beads near the interlayer interface in the as-deposited condition. The cracks can propagate along the grain boundaries and even extend across the interface into the newly deposited upper beads. The weld metal liquation cracking can be healed after the post-clad solution heat treatment. The relatively high cooling rate during laser deposition results in less Nb segregation in the deposited zone due to the insufficient time for solute redistribution. As a result, less Laves phase, and/or relatively fine, discrete Laves particles are formed. All these findings ascertain significant microstructural advantages for the laser deposits over conventional arc welds. Post-clad solution heat treatment results in partial dissolution of Laves particles at a solution temperature of 954 °C and the precipitation of needle-like δ phase around the Laves particles. The hardness of the laser deposits can be nearly recovered to the level of the as-serviced parent metal after post-clad full heat treatment. The successful deposition of integral Inconel 718 welds with no visible pores but only some minor weld metal liquation cracking indicates the great potential of using fiber laser technique by filler wire addition to remanufacture (repair) and/or manufacture superalloy components for aerospace applications.

Acknowledgments The authors are grateful to the technical support of X. Pelletier and E. Poirier for the preparation of the laser deposited coupons and metallography. Stéphane Godin is acknowledged for supporting the Brinell hardness measurements at Institut de Recherche d'Hydro-Québec.

References

1. Dupont JN, Lippold JC, Kiser SD (2009). Welding metallurgy and weldability of nickel-base alloys, book
2. Qi H, Azer M, Ritter A (2009) Studies of standard heat treatment effects on microstructure and mechanical properties of laser net shape manufactured Inconel 718. Metall Mater Trans A 40A:2410–2422
3. Baufeld B (2011) Mechanical properties of Inconel 718 parts manufactured by shaped metal deposition (SMD). J Mater Eng Perform 21(7):1416–1421

4. Ram GDJ, Reddy AV, Rao KP, Reddy GM, Sundar JKS (2005) Microstructure and tensile properties of Inconel 718 pulsed Nd-YAG laser welds. J Mater Process Technol 167:73–82
5. Ram GDJ, Reddy AV, Rao KP, Reddy GM (2005) Microstructure and mechanical properties of Inconel 718 electron beam welds. Mater Sci Technol 21(10):1132–1138
6. Cao X, Rivaux B, Jahazi M, Cuddy J, Birur A (2009) Effect of pre- and post-weld heat treatment on metallurgical and tensile properties of Inconel 718 alloy butt joints welded using 4 kW Nd:YAG laser. J Mater Sci 44(17):4557–4571
7. Fontana G, Gobbi S, Rivela C, Zhang L (1999) Laser welding in the manufacture of superalloy components. Weld Int 13(8):631–635
8. Gobbi S, Zhang L, Norris J, Richter KH, Loreau JH (1996) High powder CO_2 and Nd-YAG laser welding of Wrought Inconel 718. J Mater Process Technol 56(1–4):333–345
9. Gobbi SL, Li Z, Norris I (1994) An investigation on the techniques and metallurgy in laser welding of Wrought 718, in Eurojoin 2. European Conference and Joining Technology, Florence, pp 655–665
10. Zhong ML, Sun HQ, Liu WJ, Zhu XF, He JJ (2005) Boundary liquation and interface cracking characterization in laser deposition of Inconel 728 on directionally solidified Ni-based superalloy. Scr Mater 53:159–164
11. Quintino L, Costa A, Miranda R, Yapp D (2007) Welding with high power fiber lasers—a preliminary study. Mater Des 28(4):1231–1237
12. Gregorcic P, Mozina J (2009), High Power Fiber Lasers, Postgraduate Seminar, Department of physics, University of Ljubljana
13. Vollertsen F, Thomy C (2005) Welding with fibre lasers from 200 to 17000 W. ICALEO 2005-24th International Congress on Applications of Laser and Electro-Optics, Miami, pp 254–263
14. Chen HC, Pinkerton A, Li L (2011) Fibre laser welding of dissimilar alloys of Ti-6Al-4V and Inconel 718 for aerospace applications. Int J Adv Manuf Technol 52:977–987
15. Borges B, Laser cladding using filler powder and wire, master thesis, Mechanical Engineering, Universidade Tecnica de Lisboa
16. Ion JC (2005) Laser processing of engineering materials; principles. Procedure and industrial application. Elsevier Butterworth-Heinemann, Hoboken
17. Kim JD, Peng Y (2000) Plunging method for Nd:YAG laser cladding with wire feeding. Opt Lasers Eng 33:299–309
18. Processing of Engineering Materials (2005); *Principles*, *procedure and industrial application*, Elsevier Butterworth-Heinemann, Hoboken
19. Richter K, Bostanjoglo G, Dommaschk R, Mayrhofer R, Pathe D, Weber H (1995) Comparative Study on Aluminum and Steel Welding with CW and Repetitively Q-Switched Nd:YAG Lasers. Soc Opt Eng Cleve Ohio 2789:12–20
20. Duley WW (1999) Laser welding. Wiley, Toronto
21. Hooijmans JW, Lippold JC, Lin W (1997), Effect of Multiple Postweld Heat Treatment on the Weldability of Alloy 718. Superalloys 718, 625, 706 and Various Derivatives. Ed. By Ea Loria, TMS
22. Brooks JW, Bridges PJ (1988). Metallurgical stability of Inconel Alloy 718, superalloys, ASM International , Materials Park, OH, pp. 33–42
23. Quested PN, McLean M (1980), Effect of variations in temperature gradient and solidification rate on microstructure and creep behaviour of IN738 LC, Solidification Technology in the Foundry and Cast House, The Metals Society Coventry England, pp. 586
24. Osoba LO, A Study on Laser Weldability Improvement of Newly Develop Haynes 282 Superalloy, PhD thesis, Department of Mechanical and Manufacturing Engineering, University of Manitoba
25. Kou S (2002). Welding metallurgy, Wiley, Hoboken
26. Knorovsky GA, Cieslak MJ, Headley TJ, Romig AD, Hammetter WF (1989) Inconel 718: a solidification diagram. Metall Mater Trans A 20A:2149–2158
27. Radhakrishna CH, Rao KP (1997) The formation and control of laves phase in superalloy 718 welds. J Mater Sci 32:1977–1984
28. Biswas S, Reddy GM, Mohandas T, Murthy CVS (2004) Residual stresses in Inconel 718 electron beam welds. J Mater Sci 39:6813–6815
29. Radavich JF (1989). The physical metallurgy of cast and wrought alloy 718, Conference Proceedings on Superalloy 718—metallurgy and applications, The Minerals, Metals & Materials Society, pp. 229–240
30. Lippold JC, Clark WAT, Tumuluru M (1992). An investigation of weld metal interfaces, The metal Science and Joining, Edited by M.J. Cieslak, J.H. Perepezko, S. Kang and M.E. Glicksman, The Minerals, Metals & Materials Society
31. Thompson RG, Dobbs JR, Mayo DE (1986) The effect of heat treatment on microfissuring in Alloy 718. Weld J 65(11):299s–304s
32. Chaturvedi MC (2007) Liquation cracking in heat affected zone in ni superalloy welds. Mater Sci Forum 546–549:1163–1170